

Article

Mechanical Behavior of Precast Circular Semi-Continuous CFST Columns under a Uniaxial Eccentric Load

Bing Cao ^{1,2,3,*}, Longfei Zhu ^{1,2}, Huashan Qian ^{1,2} and Zhicheng Pan ^{1,2,4,5,*}

¹ School of Architecture and Civil Engineering, Anhui Polytechnic University, Wuhu 241000, China; frogcrow147@gmail.com (L.Z.); 2221410102@stu.ahpu.edu.cn (H.Q.)

² Engineering Research Center of Anhui Green Building and Digital Construction, Anhui Polytechnic University, Wuhu 241000, China

³ Engineering Research Center of Anhui Metallurgical Solid Waste Green Construction, Anhui University of Technology, Ma'anshan 243032, China

⁴ Sinohydro Engineering Bureau 8 Co., Ltd., Changsha 410004, China

⁵ Power China Chizhou Changzhi Prefabricated Construction Co., Ltd., Chizhou 247100, China

* Correspondence: caobing.0427@ahpu.edu.cn (B.C.); panzhichengcsu@163.com (Z.P.)

Abstract: For this study, we conducted a detailed examination and comprehensive comparative analysis of the structural responses and mechanical behavior of bolted sleeve connections in precast circular semi-continuous steel tubular concrete (PCSCFST) columns. The research involved fourteen specimens, and we considered the impacts of various parameters, including eccentricity, external steel sleeve thickness, bolt diameter, and slenderness ratio. The findings revealed that the external steel sleeve significantly enhances the protection of the connection area, enabling the bolts to effectively withstand eccentric loads. However, sleeves that are too thick may lead to premature bolt failure, reducing their ultimate load-bearing capacity. Using bolts to transfer loads to the concrete significantly strengthens the restraining effect of the steel sleeve. Nonetheless, increasing the bolt diameter beyond a certain threshold may diminish this beneficial impact, potentially leading to connection failure and a decrease in ultimate load-bearing capacity. A new 'cooperative value q ' measures component collaboration at ultimate capacity, showing that shorter columns offer less effective coordination than longer ones. Through regression analysis, we formulated a prediction for axial ultimate bearing capacity, closely aligning with the experimental data (N_{pre-a}/N_u average value of 1.003, variance 0.00248). Three N - M curves, including the Eurocode 4 method, offered conservative predictions, with Eurocode 4 closely matching the experimental results. A refined prediction method following Eurocode 4 was developed, yielding an average P_{pre-U}/P_u value of 0.971 and a variance of 0.0107.

Keywords: PCSCFST column; compression bearing capacity; slenderness ratio; relative eccentricity; N - M interaction curve



Citation: Cao, B.; Zhu, L.; Qian, H.; Pan, Z. Mechanical Behavior of Precast Circular Semi-Continuous CFST Columns under a Uniaxial Eccentric Load. *Buildings* **2024**, *14*, 772. <https://doi.org/10.3390/buildings14030772>

Academic Editor: Elena Ferretti

Received: 8 February 2024

Revised: 1 March 2024

Accepted: 5 March 2024

Published: 13 March 2024

Correction Statement: This article has been republished with a minor change. The change does not affect the scientific content of the article and further details are available within the backmatter of the website version of this article.



Copyright: © 2024 by the authors. Licensee MDPI, Basel, Switzerland. This article is an open access article distributed under the terms and conditions of the Creative Commons Attribution (CC BY) license (<https://creativecommons.org/licenses/by/4.0/>).

1. Introduction

Due to their superior fire resistance, seismic stability, and high load-bearing capacity, concrete-filled steel tubes (CFSTs) have increasingly become the preferred choice for high-rise buildings, large structures, and bridges [1,2]. However, as CFST components are individually manufactured, strategically designed connections are necessary for practical construction to achieve structural integration, whether involving CFST-to-CFST connections or connections between CFSTs and cast-in-place structures.

Moreover, the complex nature of component junctions necessitates a thorough scholarly investigation into CFST connectivity issues. As a result, numerous scholars have undertaken studies to address the connection challenges associated with CFSTs [3–8]. Song et al. [9] explored load introduction and transfer mechanisms in K-type connections in steel-encased CFSTs, while Zhou et al. [10] brought innovation to the design of circular

CFST pier connections known as CECCs. Xu et al. [11] proposed a novel anchor-rebar-column-foundation connection (SAC) tailored for CFST columns, and M. Ansari et al. [12] undertook a numerical analysis of the performance of a rib stiffener steel beam connected to a circular CFST column under cyclic loading conditions. Additionally, Lei et al. [13] introduced a novel fully welded concrete-filled integral K-joint with longitudinal preformed ribs to enhance fatigue performance, and Sun et al. [14] delved into the local and post-local buckling behavior of welded square high-strength steel tubes with concrete-infilled restraints. Further contributions include Liu et al. [15], who designed a T-shaped irregular CFST column by welding I-shaped and U-shaped steel components together and assessed their flexural stability under combined axial loads and moments. Lin et al. [16] presented a new generation of through-diaphragm bolted-welded joints to connect narrow cross-section CFST columns to H-beams, utilizing both bolts and welding techniques for enhanced security. Tong et al. [17] investigated the bending moment capacity of beam-to-wall connections employing both flanges and bolts, and Ali Parvati et al. [18] examined the behavior achieved by connecting a beam with a drilled flange to a CFST steel column through numerical simulations. Piseth Doung et al. [19] researched the mechanical behavior of wide-flange (WF) beam-to-box column connections, assessing the tensile strength and failure mechanisms and noting a connection strength improvement of roughly 30% in concrete-filled specimens over those without concrete. Wei Hong Ng et al. [20] studied the tensile mechanical behavior of blind bolts in CFST connections, finding that a well-designed anchorage system could significantly enhance the stiffness and tensile capacity of the connections. Wu et al. [21] introduced a novel design for bolted beam-to-column connections in CFST structures, showcasing a superior seismic resistance through enhanced stiffness, strength, ductility, and energy dissipation mechanisms. Gan et al. [22] proposed an innovative demountable linkage mechanism for interconnecting upper and lower CFST columns, showing a favorable ductility performance and minimal impact on the seismic response after service loading, disassembly, and reassembly. Finally, Yang et al. [23] assessed the axial and flexural strengths of column splices in nineteen specimens, providing recommendations for the optimal selection and detailing of these splices.

Significant research efforts, including those by Song et al. [9] through Yang et al. [23], have explored various aspects of CFST connections, ranging from load transfer mechanisms and design innovations to the performance of novel connection methods under specific loading conditions. These studies have significantly advanced our understanding of CFST connection behavior and performance; however, challenges persist, particularly concerning stress concentration, force transmission, and concrete strength utilization in existing connection methods such as flange connections, weld joint connections, and bolted connections. Flange connections often result in the force being concentrated on the steel tube, potentially inducing buckling and undermining the practical confinement effects. Weld joint connections may lead to stress concentration at the weld zone, rendering them susceptible to fatigue failure. Similarly, bolted connections can cause stress concentration at the bolts' upper ends within the concrete, limiting the effective utilization of concrete strength. These limitations underscore the need for innovative connection approaches to mitigate these issues.

This study introduces a novel bolt-sleeve connection method, designed to address the highlighted challenges by offering improved flexibility and load distribution in beam-to-column connections. The method integrates an external steel sleeve to enhance the hoop effect at the connection point, thus facilitating a more balanced load distribution between the concrete and the steel tube. Focusing on the fundamental column-column connection, for this study, we conducted uniaxial eccentric loading tests to thoroughly investigate the collaborative performance of the components within this connection method and their influence on the overall structural mechanics. A circular column-beam connection node and a square column-beam connection node employing this method are depicted in Figure 1, illustrating a practical application of the proposed method.

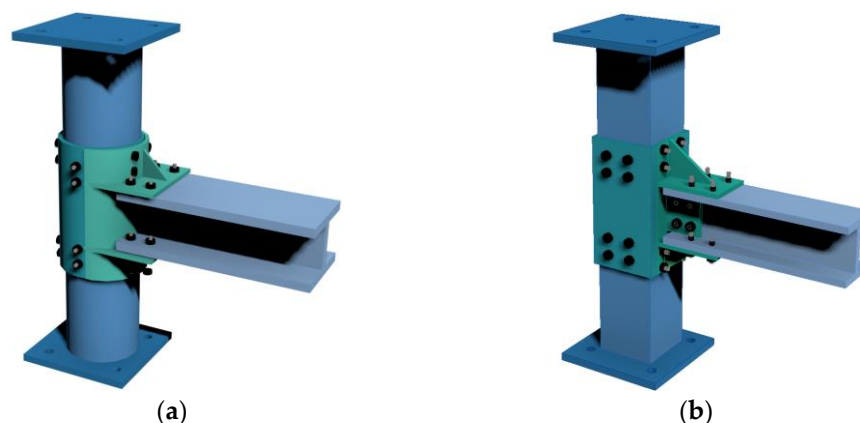


Figure 1. The proposed connection method using the bolt-sleeve technique. (a) Circular column–beam connection node. (b) Square column–beam connection node.

Our comprehensive study encompassed the design and analysis of 14 PCSCFST columns with variations in slenderness ratios, relative eccentricity, steel tube thickness, and other vital parameters. These test specimens comprised two sections of CFST column, securely joined by external steel sleeves fastened with bolts, as illustrated in Figure 2. Notably, as shown in Figure 2, the frontal section of the external steel sleeve was rendered visibly transparent for optimal observational convenience. The experimental phase involved subjecting these specimens to uniaxial eccentric compression testing. Furthermore, our investigation explored the calculation methods for N – M interaction curves to determine the ultimate bearing capacity of the PCSCFST columns.

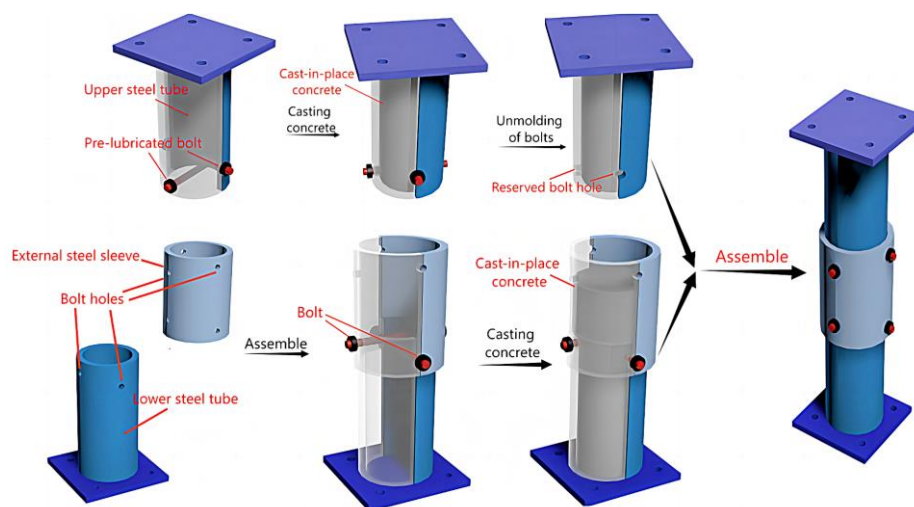


Figure 2. Column–column specimen connected using the bolt-sleeve method.

2. Experimental Programs

2.1. Specimens

A total of 14 PCSCFST column specimens were prepared and subjected to failure tests under eccentric compression. For each specimen, the upper and lower halves of the CFST columns were individually cast in place from concrete and then assembled after 28 days of curing in the laboratory. The length of the external steel sleeve for all specimens was consistently set at 200 mm. All columns were designed with different parameters, including the slenderness ratio, the diameter of the bolt, the eccentricity of loading, the thickness of the steel tube, and the thickness of the external steel sleeve. Each specimen utilized high-strength bolts of grade 8.8. These specimens were numbered PCSCFST1~PCSCFST10, while the comparison specimens were numbered PCSCFST11~PCSCFST14. The details of

the specimens are presented in Table 1, and the specific dimensions of the specimens are depicted in Figure 3. The specimens were also categorized into nine groups according to the different parameters, as indicated in Table 2.

Table 1. Details of the specimens.

| Specimen No. | e (mm) | t (mm) | D_1 (mm) | D (mm) | t_1 (mm) | d (mm) | L_1 (mm) | L_2 (mm) | L (mm) | λ |
|--------------|----------|----------|------------|----------|------------|----------|------------|------------|----------|-----------|
| PCSCFST1 | 32 | 5 | 140 | 150 | 4.75 | 12 | 220 | 200 | 490 | 13 |
| PCSCFST2 | 32 | 5 | 140 | 150 | 5 | 12 | 220 | 200 | 490 | 13 |
| PCSCFST3 | 64 | 5 | 140 | 150 | 4.75 | 12 | 220 | 200 | 490 | 13 |
| PCSCFST4 | 64 | 6 | 140 | 152 | 5 | 12 | 220 | 200 | 490 | 13 |
| PCSCFST5 | 48 | 5 | 140 | 150 | 4.75 | 12 | 220 | 200 | 490 | 13 |
| PCSCFST6 | 64 | 5 | 140 | 150 | 5 | 12 | 220 | 200 | 490 | 13 |
| PCSCFST7 | 64 | 5 | 140 | 150 | 8 | 12 | 1200 | 200 | 2450 | 64 |
| PCSCFST8 | 64 | 5 | 140 | 150 | 5 | 12 | 1200 | 200 | 2450 | 64 |
| PCSCFST9 | 32 | 5 | 140 | 150 | 8 | 12 | 1200 | 200 | 2450 | 64 |
| PCSCFST10 | 64 | 5 | 140 | 150 | 5 | 18 | 1200 | 200 | 2450 | 64 |
| PCSCFST11 | 0 | 5 | 140 | 150 | 4.75 | 12 | 220 | 200 | 490 | 13 |
| PCSCFST12 | 0 | 6 | 140 | 152 | 5 | 12 | 220 | 200 | 490 | 13 |
| PCSCFST13 | 0 | 5 | 140 | 150 | 5 | 12 | 220 | 200 | 490 | 13 |
| PCSCFST14 | 0 | 5 | 140 | 150 | 5 | 12 | 1200 | 200 | 2450 | 64 |

Note: e is eccentricity, t is thickness of steel tube, D_1 is diameter of column, D is diameter of concrete core, t_1 is thickness of the external steel sleeve, d is diameter of bolt, L_1 is length of the upper and lower column, L_2 is length of the external steel sleeve, L is length of the PCSCFST column, λ is slenderness ratio.

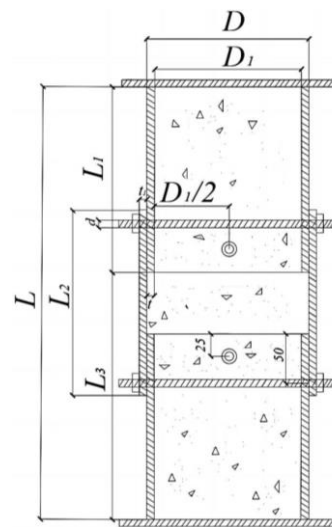


Figure 3. Geometry of the test specimens (unit: mm).

Table 2. Breakdown of the test specimens.

| Parameter | Group | Specimens | | | |
|-----------|-------|-----------|-----------|-----------|-----------|
| e | E1 | PCSCFST2 | PCSCFST6 | PCSCFST13 | PCSCFST11 |
| | E2 | PCSCFST1 | PCSCFST3 | PCSCFST5 | |
| | E3 | PCSCFST4 | PCSCFST12 | | |
| | E4 | PCSCFST7 | PCSCFST9 | | |
| | E5 | PCSCFST8 | PCSCFST14 | | |
| t_1 | T1 | PCSCFST1 | PCSCFST2 | | |
| | T2 | PCSCFST3 | PCSCFST6 | | |
| | T3 | PCSCFST7 | PCSCFST8 | | |
| d | B1 | PCSCFST8 | PCSCFST10 | | |
| λ | S1 | PCSCFST6 | PCSCFST8 | | |

2.2. Material Properties

Concrete cubes of 150 mm × 150 mm × 150 mm were cast simultaneously with the test specimens and cured for 28 days to determine the cubic strength (f_{cu}) [24]. As a result, the average cube strength f_{cu} of C30 in the specimens was 31.1 MPa.

In total, twelve tests were executed on four distinct thicknesses of tensile specimens to determine the material properties of the steel tubes (each thickness was subjected to three tests) [25]. Concurrently, six tensile bolt specimens were also examined to ascertain the material properties of the bolts. Table 3 presents the average values for the yield strength, ultimate strength, and modulus of elasticity for both the steel tube and the connecting bolt, where notations ST1 to ST4 denote the steel tube material, and BT1 to BT2 indicate the bolt material.

Table 3. Properties of the steel tubes and connecting bolts.

| Specimen | Steel Thickness (mm) | Bolt Diameter (mm) | Yield Strength (MPa) | Ultimate Strength (MPa) | Extensibility |
|----------|----------------------|--------------------|----------------------|-------------------------|---------------|
| ST1 | 4.75 | / | 372.6 | 540.1 | 27.9% |
| ST2 | 5 | / | 367.2 | 532.6 | 24.4% |
| ST3 | 6 | / | 357.8 | 525.1 | 26.4% |
| ST4 | 8 | / | 351.8 | 505.7 | 26.8% |
| BT1 | / | 12 | 811.5 | 883.3 | 8.5% |
| BT2 | / | 18 | 803.6 | 850.2 | 9.5% |

2.3. Test Setup and Instrumentation Layout

The specimens were exposed to eccentric loading tests under a 500-ton electro-hydraulic servo pressure test machine at the laboratory of Anhui Polytechnic University. The loading equipment is depicted in Figure 4. To ensure that the specimens were maintained in a uni-axial eccentric loading condition, the geometric centers of the cross-section of the specimens and the loading plate were aligned on one axis in the horizontal plane, while the other axis was utilized to apply the eccentric distances of 32 mm and 64 mm. The testing procedure was governed by a program with a predetermined loading rate, which regulated the real-time load exerted by the actuator onto the specimen through the loading plate. Initially, the tests were conducted under a load-controlled speed of 6 kN/min. Subsequently, the loading protocol was shifted to a speed-controlled mode with a rate of 0.15 mm/min when the load reached 200 kN to facilitate better observations of the specimen's late-stage data variation. The test was concluded when the peak load exhibited a reduction of at least 15%.



Figure 4. The 500-ton electro-hydraulic servo pressure test machine.

Considering the symmetry of the column, the axial symmetry of the eccentric loading, and the general trend of column strain distribution under axial pressure, 22 strain gauges were affixed to 11 measurement points throughout the PCSCFST column, with 2 strain gauges at each measurement point to capture the lateral and vertical strains at that point. A total of six measurement points were placed on both sides of the column in the direction of eccentricity, specifically at the midpoint of the upper half of the column, the midpoint of the column's lower half, and the external steel sleeve midpoint. Additionally, three measurement points were positioned on the side of the column perpendicular to the eccentricity distance. The other two strain measurement points were located at the midpoint of the bolt. The vertical displacement measurement points were situated on both sides of the plate of the upper column (perpendicular to the eccentric direction), while the lateral displacement meters were located at various locations, including, among others, the midpoint of the upper column, the midpoint of the external steel sleeve, and the midpoint of the lower column. The measurement points were numbered from top to bottom as L1 to L7, and their specific locations can be seen in Figure 5.

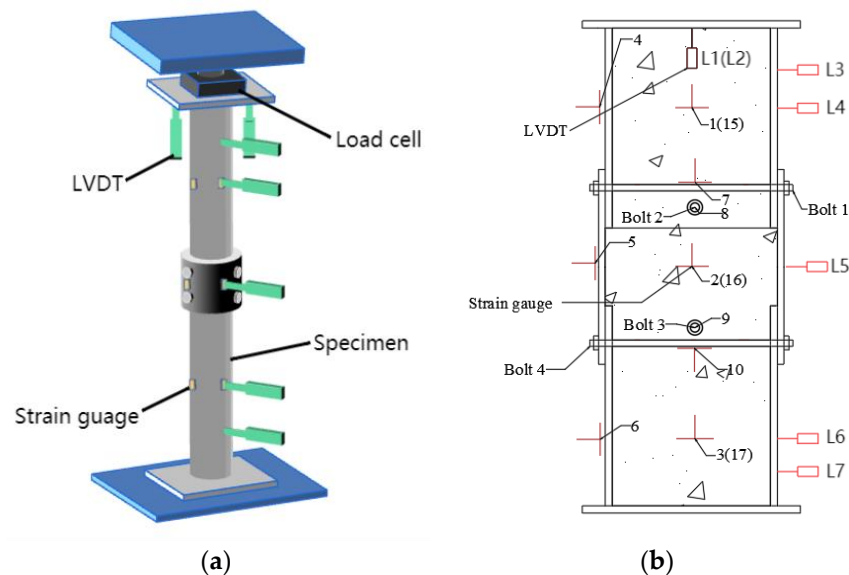


Figure 5. Test arrangements: the locations of strain gauges and LVDTs. (a) Three-dimensional diagram. (b) Two-dimensional diagram.

3. Analysis of Experimental Results

3.1. Failure Mode

The experimental results reveal that specimen failure can be categorized into two main types. The first involves local buckling, characterized by steel tube buckling and concrete crushing. The second type is overall bending, where the specimen loses stability without significant local failure. These phenomena are evident in both short columns (slenderness ratio of 13) and long columns (slenderness ratio of 64), with the failure modes grouped accordingly, as shown in Figure 6. Notably, no significant damage to the external steel sleeve was observed in any of the tests, underscoring the bolts' effective load transmission through the internal concrete. This transmission mechanism reduces the load on the external sleeve, maintaining its structural integrity and restraining capacity. The specimens marked in yellow in Figure 6 represent the axial compression specimens used for comparative analysis.

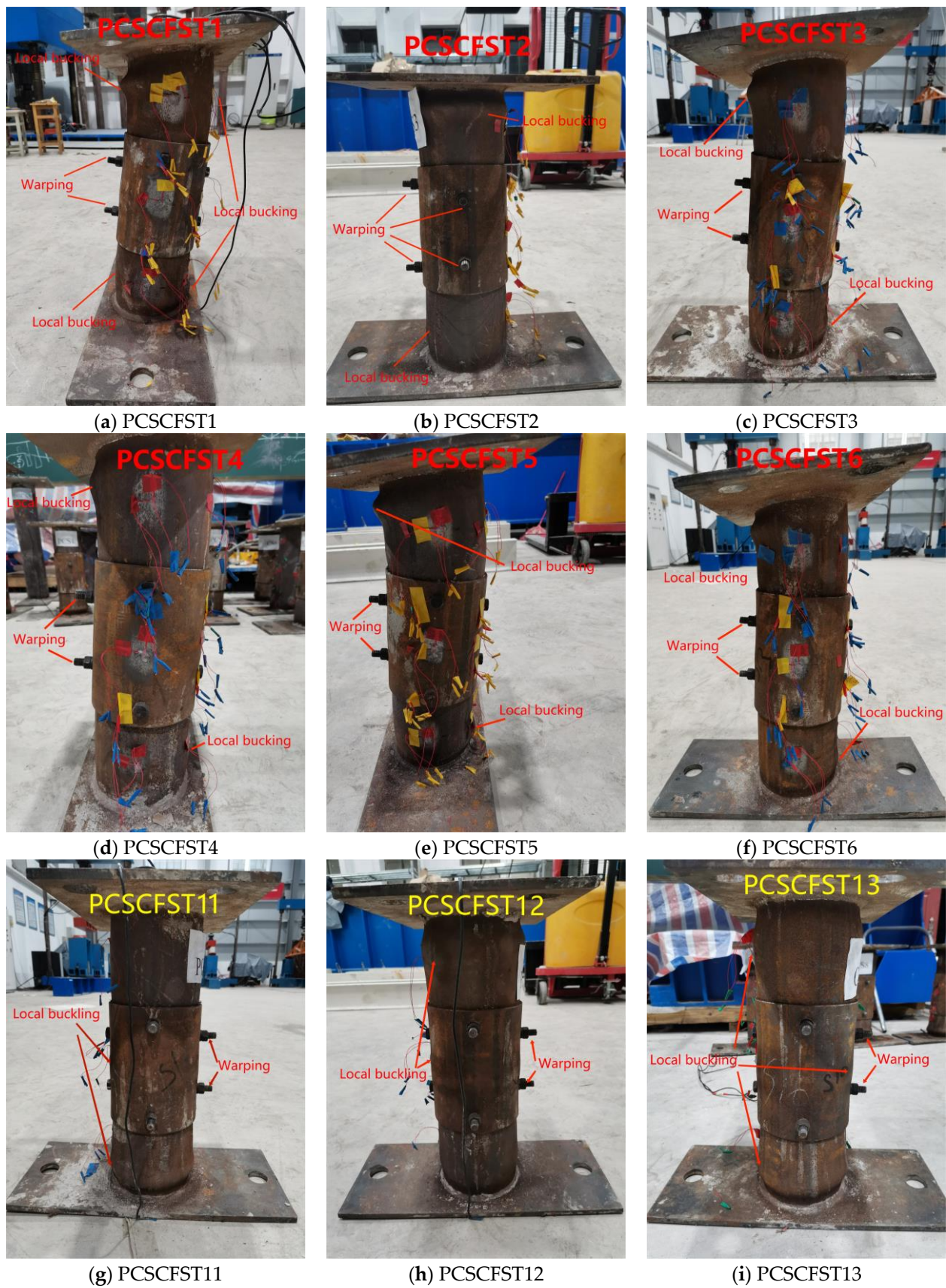


Figure 6. Cont.



Figure 6. Failure phenomena in specimens.

During the experiment, local buckling was gradually revealed between the external steel sleeve and both the upper and lower sections of the column. As loading progressed, the concrete in these areas was crushed, and the steel tube showed signs of yielding, eventually leading to pronounced annular convex or arc-shaped expansion deformation. Additionally, the ends of the bolts connecting the upper and lower steel tubes to the external steel sleeve deformed in their respective directions. This indicates that the primary force on the bolts originates from the attached steel tube. The force transmission path, therefore, runs from the upper steel tube, through the bolt, to the external sleeve, and then to the lower tube. In comparison, the long columns in PCSCFST7~10 and PCSCFST14 showed less pronounced failure than the short columns, with almost straight lower sections. The misalignment of their bending with the eccentricity direction indicates a propensity for instability failure. Under shear force, the bolt exhibited slight warping. This slight deformation occurred because the bolt was encased in concrete within the steel tube, and this structure resisted significant bending or the deformation of the bolt. Therefore, unless the bolt was sheared off at the interface between the steel tube and the external steel sleeve, significant warping was unlikely to occur.

In the short-column experiments E1–E3, local buckling was more widespread in specimens with lower eccentricity, while in those with higher eccentricity, the buckling was

concentrated on the eccentric side, suggesting a transition from uniform to concentrated stress distribution in the steel tube with increasing eccentricity. In the long-column experiments E4–E5, the irregular pattern of instability and bending failures obscured any distinct trend. Columns with thinner external steel sleeves generally showed more intense local buckling and bending than those with thicker sleeves. However, in group T3, the thicker-sleeved PCSCFST7 exhibited more severe bending than the thinner-sleeved PCSCFST8, underscoring the importance of optimal sleeve thickness for ensuring coordinated column deformation. In group B1, PCSCFST10, with a larger bolt diameter, showed more pronounced bending than PCSCFST8, suggesting the importance of setting the bolt diameter within a reasonable range. In group S1, as previously mentioned, the short-column PCSCFST6 exhibited more localized failure compared to the less pronounced failure in the long-column PCSCFST8.

3.2. Load–Axial Shortening Curves

Figure 7 displays the load–axial compression curves for different parameter-controlled specimen groups. In the short-column groups E1–E3 (Figure 7a–c), the eccentricity initially had little impact on stiffness, with no clear pattern in loading stiffness. However, specimens with a greater eccentricity yielded earlier as the load increased. For groups E4–E5, those with a higher eccentricity showed lower initial stiffness and yielded sooner than those with lower eccentricity.

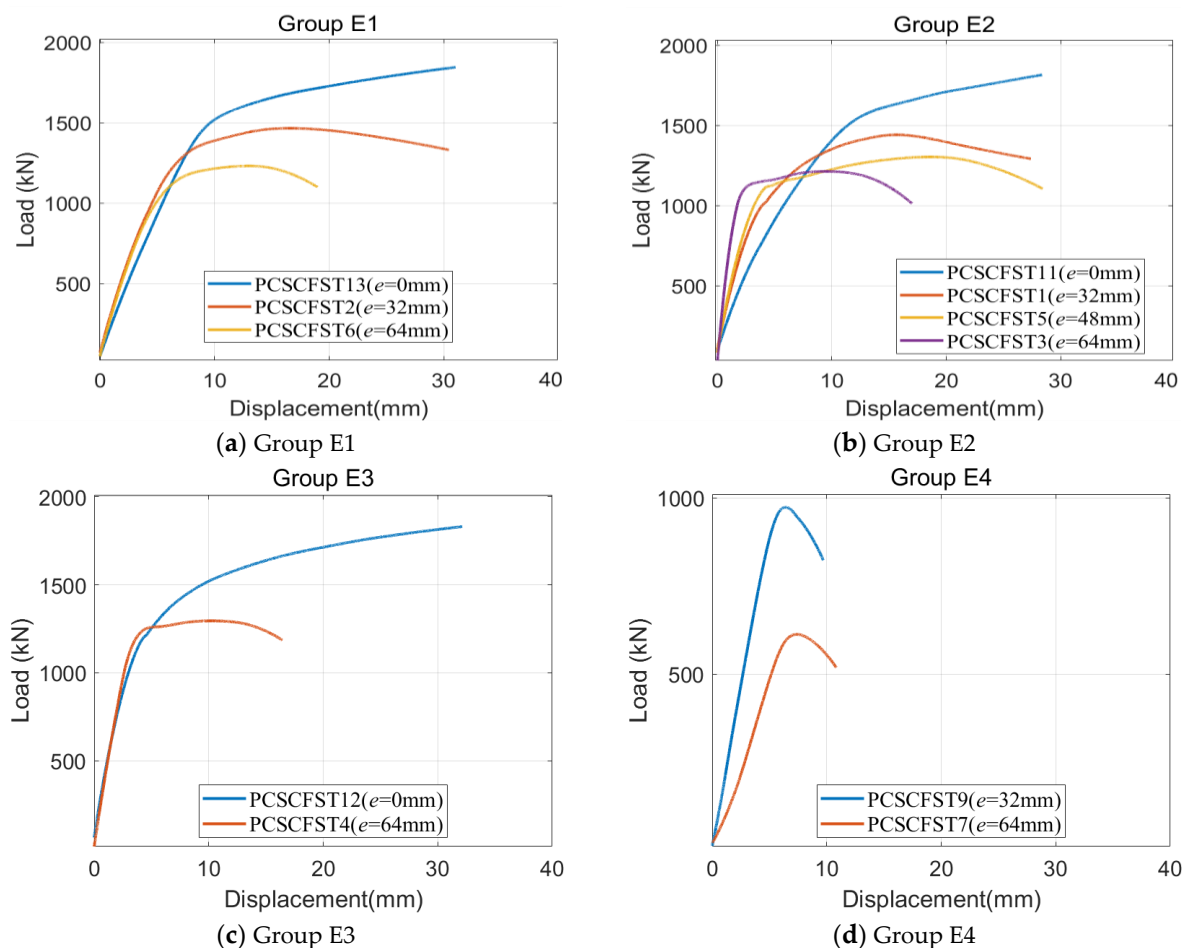


Figure 7. Cont.

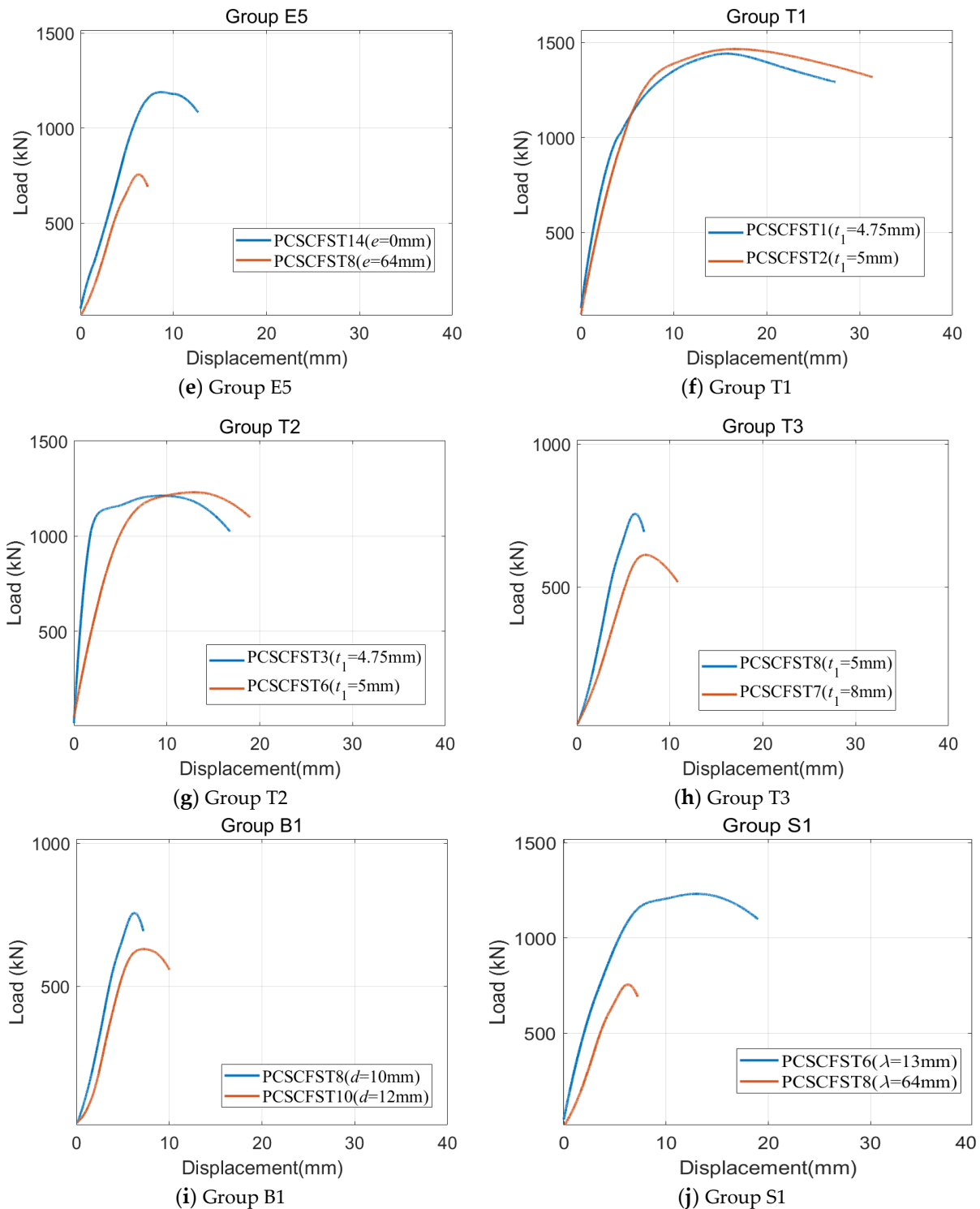


Figure 7. Load–axial shortening curves.

In brief, in short columns, the eccentricity does not greatly impact the initial stiffness, but it significantly lowers it in longer columns. This may be because, due to their shorter length, short columns tend to have a more uniform distribution of forces when subjected to loads, with eccentricity-induced bending moments being relatively minor. Consequently, the eccentricity has a negligible impact on their initial stiffness. Conversely, long columns, due to their extended length, are more susceptible to localized bending or overall instability. When eccentricity-induced moments are significant, their impact on long columns becomes

markedly evident. From the perspective of internal force distribution, the presence of eccentricity disrupts the linear or uniform distribution of internal forces. The greater the eccentricity, the more likely it is that the compressive forces will deviate from the central axis, leading to stress concentration in the compressed regions and potentially creating a stress gradient, thus affecting the initial stiffness. This effect is particularly pronounced in long columns, which are more prone to local bending, highlighting the significant influence of eccentricity in these scenarios.

Across all groups with varying eccentricities, a general pattern emerges: greater eccentricity leads to a steeper decrease in the curve's slope after yielding, thereby reducing the specimen's load-bearing capacity. This may be attributed to the fact that, after yielding, the stress concentration becomes more pronounced under conditions of high eccentricity, causing the specimen's nonlinear behavior to become more evident and resulting in a more rapid decrease in stiffness.

In group T1, increasing the thickness of the external steel sleeve from 4.75 mm to 5 mm resulted in a slight increase in ultimate bearing capacity (P_u) from 1443 kN to 1465 kN, a 1.5% difference. This minimal change is reflected in the similar slopes of the curves in Figure 7f, suggesting that the thickness variation has a marginal impact on the mechanical properties of eccentrically loaded PCSCFST columns. In contrast, group T3 showed a significant reduction in P_u (19%) and stiffness with an increase in thickness from 5 mm to 8 mm, highlighting a notable impact on the mechanical properties for more substantial thickness variations, as mentioned in [26]. This is possibly due to the excessive thickness and high rigidity of the external steel sleeve; the bolts appear to be resting on the casing, reducing the effective contact with the concrete. This results in the bolts partially transferring the force intended for the concrete to the external steel sleeve instead. However, the smaller contact area between the casing and the bolts intensifies the stress concentration, and also increases the shear force of the bolt at the interface between the external steel sleeve and the steel tube. This phenomenon of stress redistribution renders the bolts more prone to failure, ultimately reducing the ultimate bearing capacity of the column.

In group B1, increasing the bolt diameter from 12 mm to 18 mm unexpectedly reduced the ultimate bearing capacity (P_u) by 16.56%, contrary to the initial assumption that larger bolts would increase P_u . PCSCFST10, with a larger bolt diameter, showed greater plasticity than PCSCFST8, evidenced by a longer yielding stage and a steeper slope. This phenomenon might be attributed to the following phenomena. In scenarios characterized by small bolt diameters, subsequent to bolt failure, although the connectors may become inoperative, the concrete sections of the upper column, external steel sleeve, and lower column can directly interact, thereby enhancing the utilization of the concrete's compressive capabilities. However, should the concrete fail prior to other components, the pressure initially borne by the concrete would shift onto the bolts and casing, thus impeding the full exploitation of the compressive capacity of the concrete sections within each component. At the same time, the pressure on the external steel sleeve increases, which will lead to a reduction in its constraint effect, thus further affecting the pressure-bearing capacity of the concrete inside. As for the plasticity comparison between PCSCFST10 and PCSCFST8, this is evidenced by the longer yielding phase and steeper stress–strain curve. This phenomenon corroborates the aforementioned observation that a larger bolt diameter results in the redirection of pressure within the connectors towards the external steel sleeve and steel tube. Steel's superior plasticity compared to that of concrete enables the entire column to exhibit an enhanced plastic deformation capacity. This effectively explains why PCSCFST10 exhibits greater plasticity under compressive forces.

In group S1, increasing the slenderness ratio from 13 to 64 led to a 38.67% decrease in P_u for PCSCFST6 and PCSCFST8, indicating that a higher slenderness ratio lowers the ultimate bearing capacity. Detailed data are presented in Table 4.

Table 4. Details of the experimental results.

| Specimen No. | Δ_u | Max. Lateral Displacement Location | Location of Failure in the Steel Tube | q | P_u (kN) | M_u (kN.m) |
|--------------|------------|------------------------------------|---------------------------------------|--------|------------|--------------|
| PCSCFST1 | 27.56 | 47.00-26 | 2, 3, 4, 7, 8, 9, 10 | 123.72 | 1443 | 69.69 |
| PCSCFST2 | 31.60 | 42.03-23 | 2, 5, 7, 9, 10 | 55.46 | 1465 | 72.21 |
| PCSCFST3 | 17.15 | 45.07-26 | 1, 3, 4, 5, 6, 9, 10 | 56.57 | 1212 | 98.44 |
| PCSCFST4 | 16.50 | 19.35-27 | 2, 3, 4, 8, 10 | 34.21 | 1296 | 85.46 |
| PCSCFST5 | 28.62 | 43.94-26 | 1, 2, 4, 5, 6, 10 | 56.78 | 1304 | 83.05 |
| PCSCFST6 | 19.04 | 31.71-23 | 1, 2, 3, 4, 5, 6, 7, 8, 9, 10 | 66.16 | 1231 | 99.19 |
| PCSCFST7 | 10.88 | 48.65-27 | No yield | 0.01 | 612 | 61.69 |
| PCSCFST8 | 8.00 | 20.57-27 | 7, 9 | 0.03 | 755 | 61.55 |
| PCSCFST9 | 9.81 | 35.00-27 | 7, 8, 15 | 0.31 | 981 | 38.43 |
| PCSCFST10 | 10.04 | 46.34-27 | 2, 5, 15, 16 | 0.04 | 630 | 60.67 |
| PCSCFST11 | 28.49 | 28.49-25 | 1, 3, 6, 7, 8, 9, 10 | 101.72 | 1775 | 0 |
| PCSCFST12 | 32.19 | 32.19-25 | 2, 3, 4 | 107.34 | 1769 | 0 |
| PCSCFST13 | 32.48 | 35.64-24 | 7, 9, 10 | 109.58 | 1786 | 0 |
| PCSCFST14 | 12.65 | 14.99-24 | 3, 6, 7, 8 | 36.68 | 1187 | 0 |

Note: $M_u = N_u (e + \delta_u)$ denotes the ultimate resistance to the bending moment. Since there are multiple lateral displacement measurement points, there are multiple δ_u , the maximum value of which is taken as the final result. P_u is identified as the peak load for specimens showing a clear descending phase. For specimens lacking a distinct inflection point, P_u is calculated using the farthest point method described in the referenced work [27].

3.3. Load–Lateral Displacement Curves

To analyze the variations in lateral displacement across the upper column, lower column, and external steel sleeve, the load–lateral displacement curves for the measurement points L4, L5, and L6 were consolidated into a single graph. This comprehensive approach provides a deeper insight into the lateral dynamics of the specimen. Figure 8 illustrates the classic load–lateral displacement curves, where each curve represents the middle position’s lateral displacement for the upper column, the external steel sleeve, and the lower column, respectively.

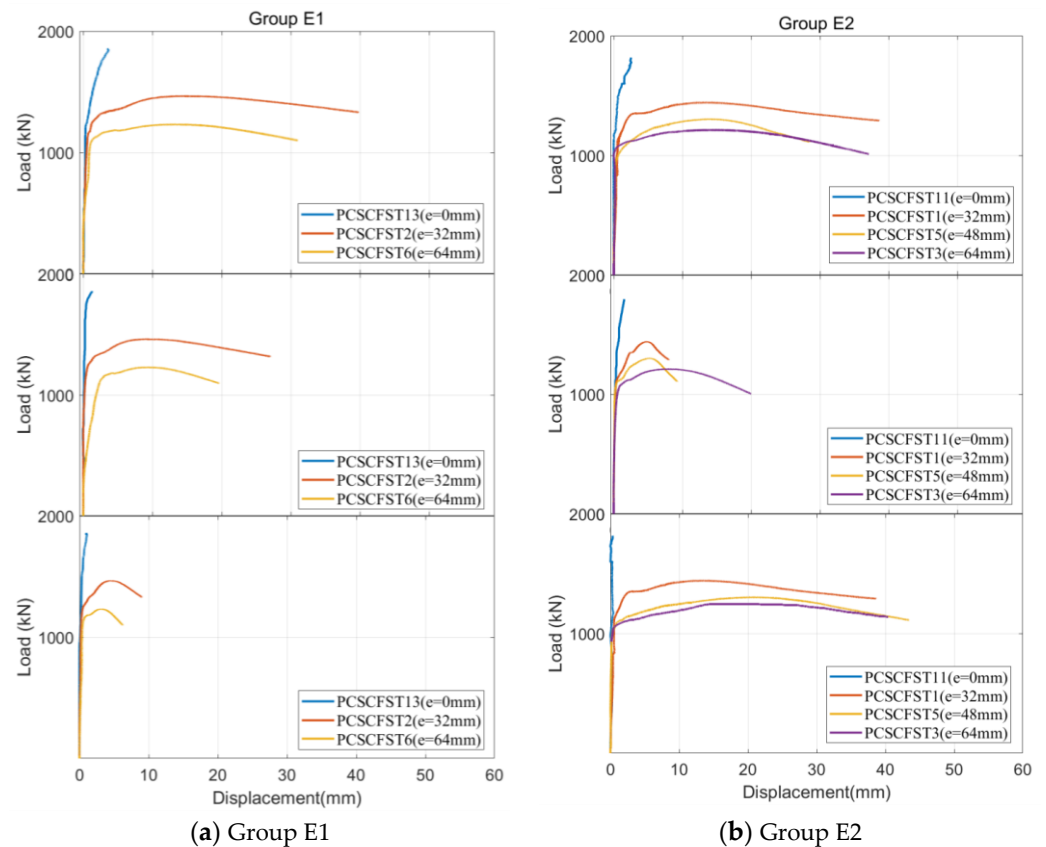


Figure 8. Cont.

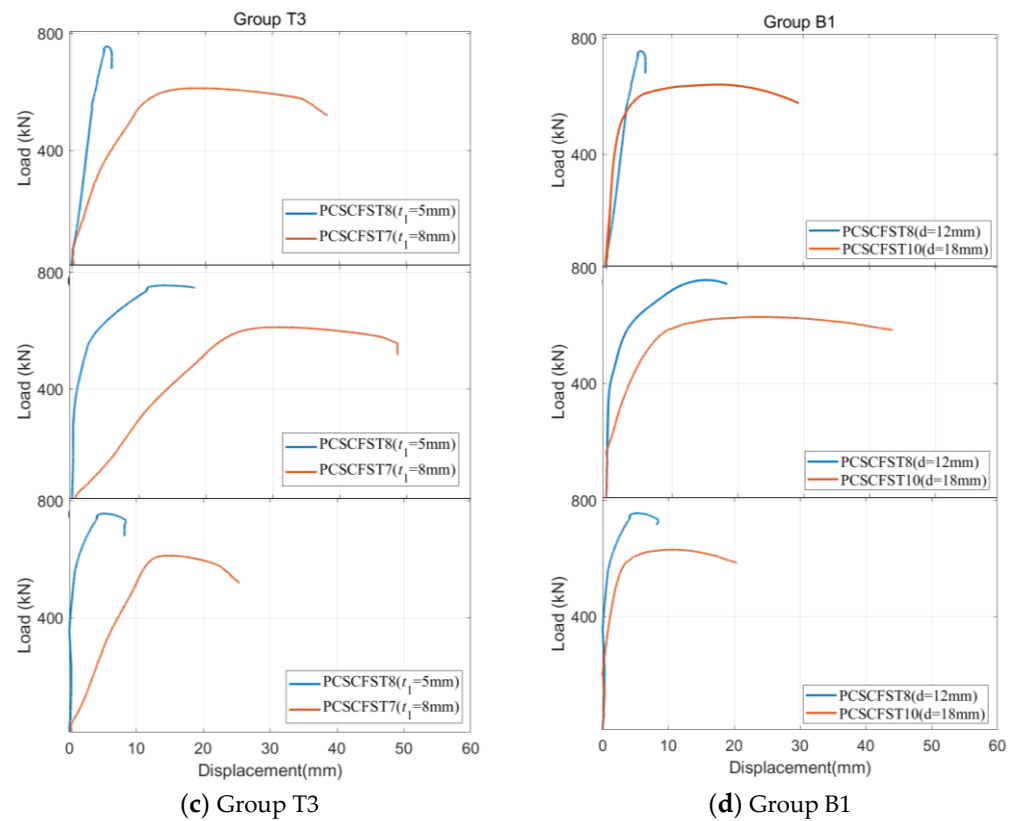


Figure 8. Axial load deflection curves for the entire column.

The load–transverse displacement curves for specimens under eccentric compression across three different sections typically exhibit a similar pattern, characterized by an initial elastic phase, followed by a transition stage and then a descent stage. Contrarily, as depicted in Figure 8a,b, the axially loaded specimen curves for both the column and the external steel sleeve lack transition and decline stages. In group T3, with the sleeve thickness increasing from 5 mm to 8 mm, there was a notable reduction in initial loading stage stiffness, leading to increased lateral displacement. In group B1, enlarging the bolt diameter from 12 mm to 18 mm resulted in a more rapid decrease in stiffness at the later stages, causing early yielding in PCSCFST10 and, ultimately, reducing the ultimate bearing capacity. This phenomenon is because, as stated above, the increase in bolt diameter alters the force transmission pathway within the connectors, leading to a greater reliance on steel tubes for load bearing. Given that the stiffness of concrete significantly surpasses that of steel tubes, this increment in bolt diameter paradoxically accelerates a reduction in stiffness in the later stages of column loading.

3.4. Load–Strain Curves for the Entire Column

Referring to [28], the axial strain (ϵ_x) and lateral strain (ϵ_y) at each point were synthesized into an equivalent strain (ϵ) using Formula (1). Figure 9 illustrates the load–strain curve for the entire specimen. (In Figure 9, the positive and negative x-axes are used only to distribute the curve evenly on both sides, without implying the tensile or compressive nature of the strain.)

$$\epsilon = \frac{\sqrt{2}}{2} \sqrt{(\epsilon_x - \epsilon_y)^2 + \epsilon_x^2 + \epsilon_y^2} \quad (1)$$

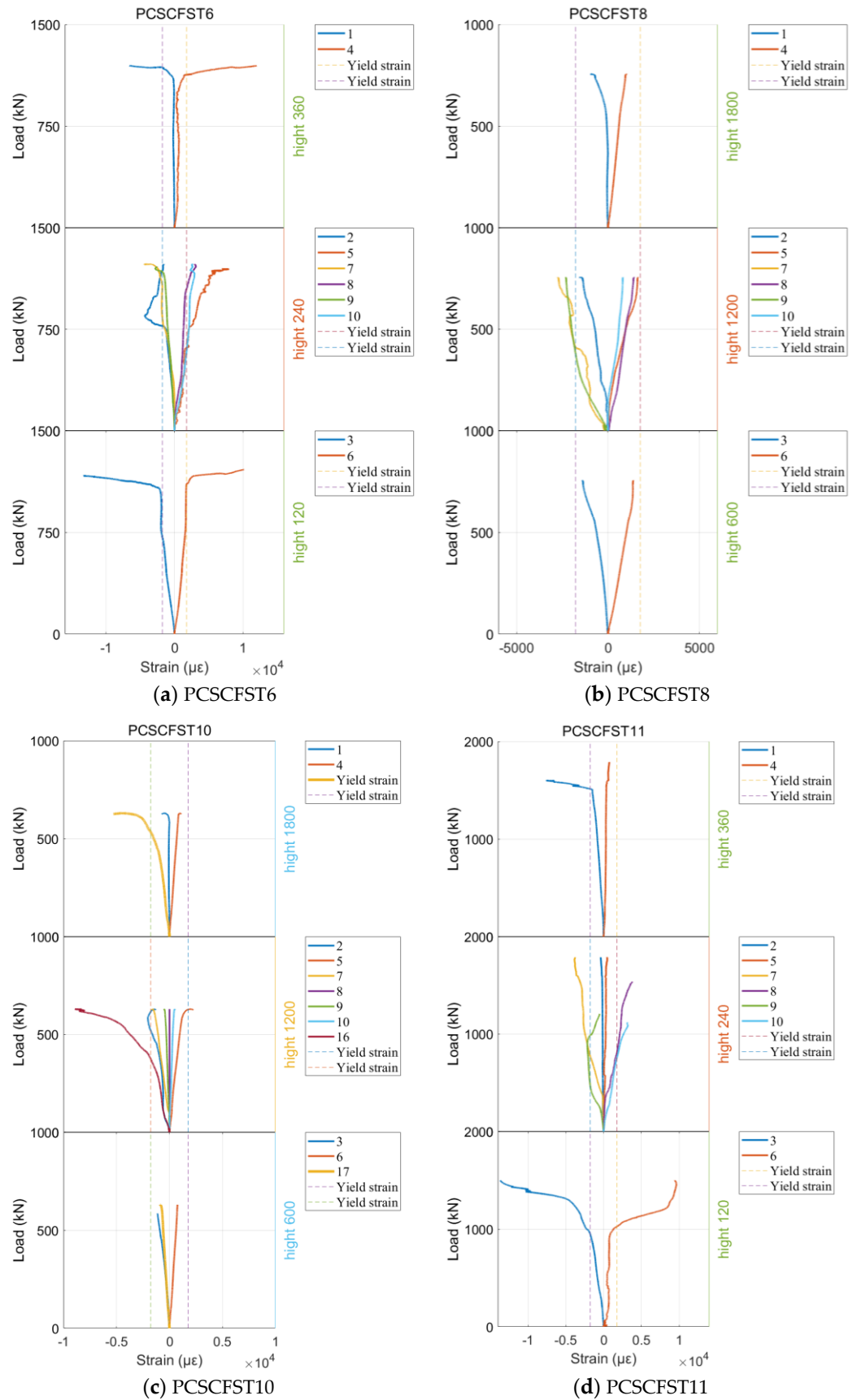


Figure 9. Cont.

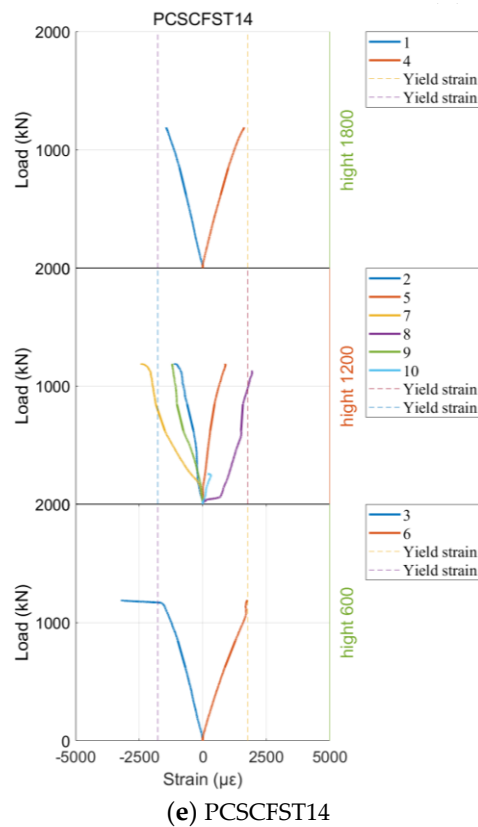


Figure 9. Typical column strain.

Each graph in Figure 9 consists of three x-axis plots representing the three heights where the strain gauges were distributed, which were 120 mm, 240 mm, and 360 mm in the short columns and 600 mm, 1200 mm, and 1800 mm in the long columns.

Figure 9 indicates that in the early loading phase, strains in both the upper and lower columns, and between the bolt and external steel sleeve, develop uniformly. However, the strain in the bolt and sleeve shows more fluctuation and does not linearly correspond to the load, suggesting that their load–strain relationship is more complex. This also reflects better coordination between the bolt and sleeve, with more consistent deformation, compared to the upper and lower steel tubes. As the load increases, the strain on the bolts and external steel sleeves accelerates. Except for PCSCFST10, all the other columns' bolt strains reached yield, indicating the full utilization of the bolt strength. In PCSCFST10, the absence of bolt yielding suggests underutilized bolt strength, despite the provision of adequate support. The larger bolt diameter in PCSCFST10, however, diminished the internal concrete section, leading to a lower load capacity compared to that of PCSCFST8 with a smaller bolt diameter. Thus, PCSCFST10 shows suboptimal coordination between the concrete and steel components at peak load capacity.

3.5. Synergy Analysis

The bolt–sleeve connection method integrates bolts, casings, and both the upper and lower columns, and cooperation among these components is crucial. Mechanically, to quantify this cooperative interaction, the 'cooperative value q ' is introduced, representing the dispersion of yield strain across different parts at the specimen's ultimate bearing capacity. Currently, ' q ' primarily considers the strain in critical steel tube sections, as measuring the internal concrete strain is challenging. The formula for calculating ' q ' is as follows:

$$q = \frac{1}{n-1} \left(\sum (\varepsilon_i - \bar{\varepsilon})^2 \right) \times 10^{-8} \quad (2)$$

where ε_i represents the strain at different positions, i represents the strain position, n represents the number of strain positions, and $\bar{\varepsilon}$ indicates the average value for the strain.

A higher ‘ q ’ value indicates a more dispersed strain among different parts at the specimen’s ultimate bearing capacity, implying less coordination among components. Conversely, a lower ‘ q ’ value suggests that the components work more harmoniously together when the specimen reaches its ultimate bearing capacity.

Table 4 presents the ‘ q ’ values for each column. Figure 10 illustrates position–strain diagrams at the ultimate bearing capacities for selected columns. In this diagram, the x-axis denotes the strain position, while the y-axis represents the strain magnitude. A blue line parallel to the x-axis marks the yield strain. Generally, specimens are expected to have yielded entirely before reaching their ultimate bearing capacity, indicating that, ideally, all strains at this point should be at yield. Any position not yet at yield suggests the underutilization of strength, whereas excessive yielding (where the strain significantly exceeds the yield point) indicates insufficient strength at that position.

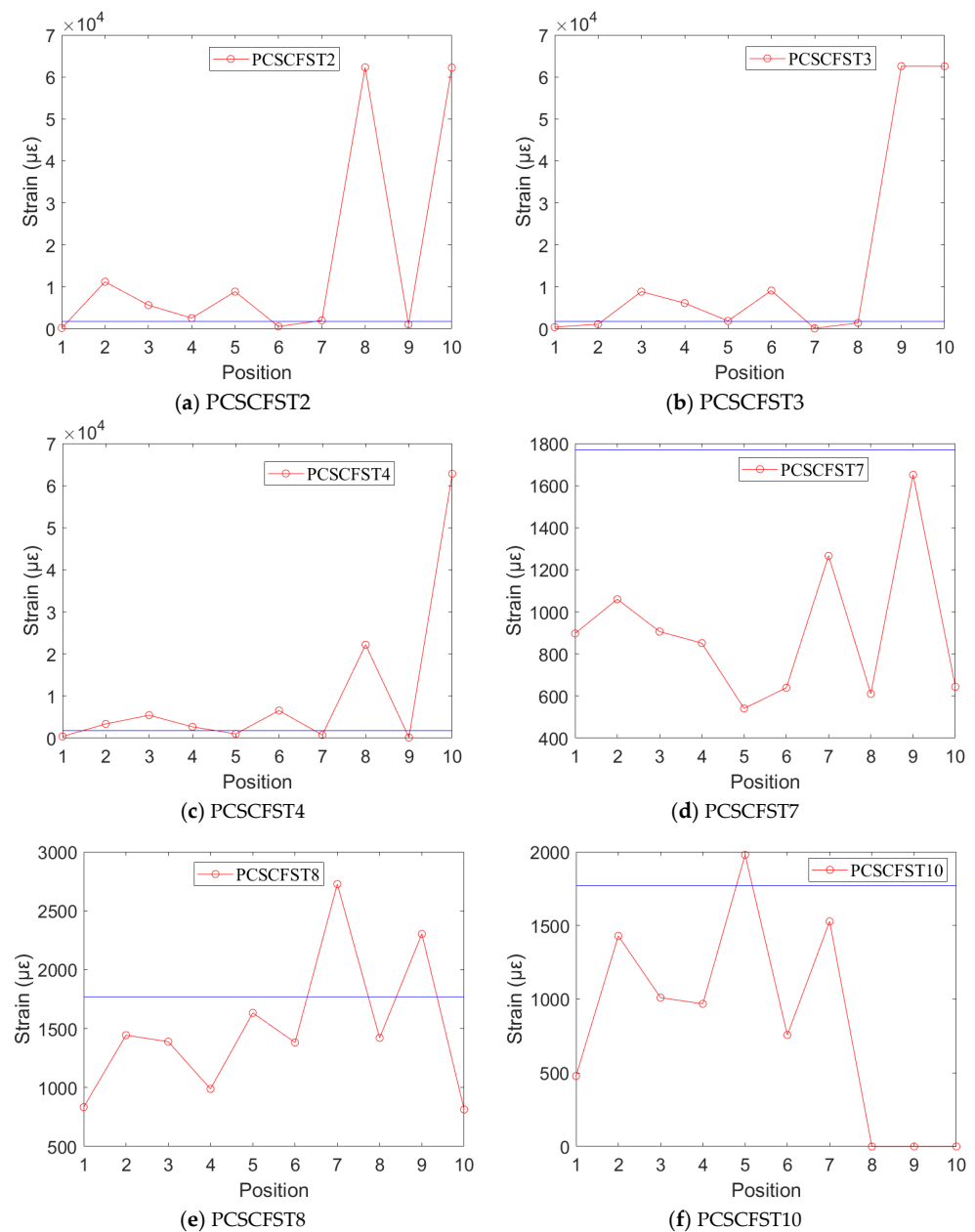


Figure 10. Collaboration–location curves for several columns under the ultimate bearing capacity.

The analysis of Table 4 reveals that ‘ q ’ values are generally lower for long columns compared to short columns, indicating better deformation coordination in the steel tube components of long columns. In the case of short columns like PCSCFST2 and PCSCFST4, the strains in steel tubes and external sleeves are relatively coordinated, but sudden changes in some bolts’ strains led to larger ‘ q ’ values. Furthermore, almost all strains in short columns reached yield at ultimate load. In contrast, long columns such as PCSCFST8 and PCSCFST10 show limited yielding, with PCSCFST7 not having yielded at all.

In short columns, the bolt strength was often inadequate, as indicated by high bolt strains and increased ‘ q ’ values, except in PCSCFST10, with thicker bolts. This led to premature bolt yielding and a lack of load-bearing coordination. Figure 10b shows that PCSCFST10’s bolts did not reach the yield strain, suggesting underutilized bolt strength but increased reliance on the external steel sleeve. For PCSCFST7, the strain coordination was ideal, with no parts reaching yield strain and a ‘ q ’ value of only 0.01, indicating internal concrete failure as the primary reason for the reduced final bearing capacity. In PCSCFST10, only one steel tube position yielded, implying underutilized steel tube strength and a weakened internal concrete cross-section, resulting in the reduced final bearing capacity.

In conclusion, increasing the bolt diameter (from 12 mm to 18 mm) leads to higher strain on the external steel sleeve, thereby facilitating earlier yielding. On the other hand, thickening the external steel sleeve (from 5 mm to 8 mm) tends to increase concrete breakage and reduce the strain in both the steel tube and the sleeve. This interplay of parameters creates a complex scenario of cooperative work among different components. For a more comprehensive analysis, additional data are necessary and could be supplemented by finite element simulations.

4. N – M Interaction Curves for PCSCFST Columns

4.1. Regression Analysis of Axial Compression Ultimate Bearing Capacity

Given that the PCSCFST column is a semi-continuous structure, traditional methods for calculating the axial compression bearing capacity of CFST columns are inadequate. To develop an N – M interaction curve for PCSCFST columns, it is essential to first derive a formula for their axial ultimate bearing capacity. Although PCSCFST columns are a novel research subject, they fall within the concrete-filled steel tube category. Their ultimate bearing capacity is still fundamentally linked to the steel tube and concrete areas. Considering parameters like the bolt diameter (d), eccentricity (e), and slenderness ratio (λ), an axial ultimate bearing capacity prediction, Formula (2), has been derived through regression analysis based on the data from reference work [26].

$$N_{pre-a} = 1.92f_y\pi(D_1^2 - D^2) \times 10^{-4} + f_c\pi D^2(74.5d - 1.25d\lambda + 9.08\lambda) \times 10^{-6} \quad (3)$$

where N_{pre-a} is the predicted value for the ultimate bearing capacity.

The predicted outcomes for the axial compression ultimate bearing capacity of the PCSCFST column are presented in Figure 11, where ‘ N_{u-a} ’ represents the experimental value of this capacity. The data suggest that the prediction made by Formula (3) closely aligns with the actual experimental results, indicating its accuracy.

4.2. The Existing N – M Interaction Curves for Cast-in-Place Columns

Simplified graphs for N – M interaction curves are provided in Eurocode 4 [29], AISC 360 [30], and the Chinese code GB 50936 [31]. These graphs use the ultimate bearing capacity and ultimate bearing moment as the y-axis and x-axis, respectively. Critical points, such as those representing the pure bending or axial compression states of PCSCFST columns, can be calculated to construct these simplified curves. Figure 12 illustrates these curves in Eurocode 4, with point A denoting axial compression, point B indicating pure bending, and the horizontal coordinate of point C representing the maximum bending moment. Notably, AISC 360’s approach to N – M interaction curves closely mirrors that of Eurocode 4. The methodology for calculating critical points in both AISC 360 and Eurocode 4 is detailed in [21], and the corresponding formula is given below.

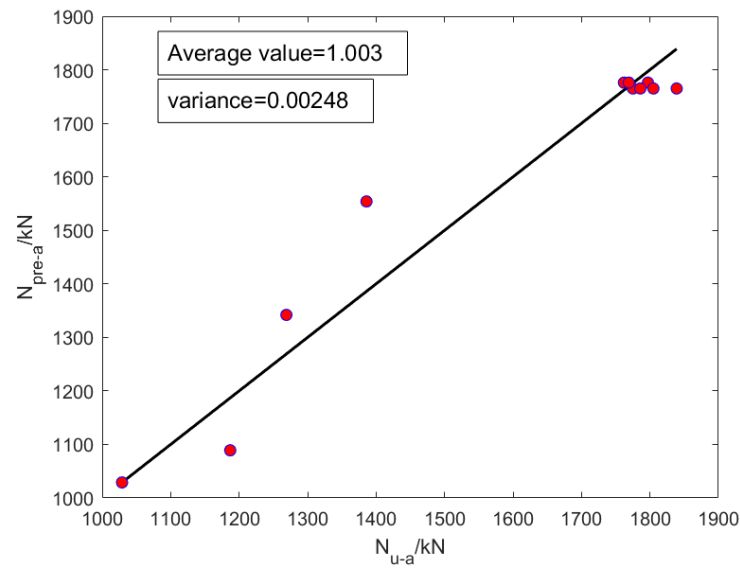


Figure 11. Comparison between the theoretical calculation and experiment for the ultimate bearing capacity.

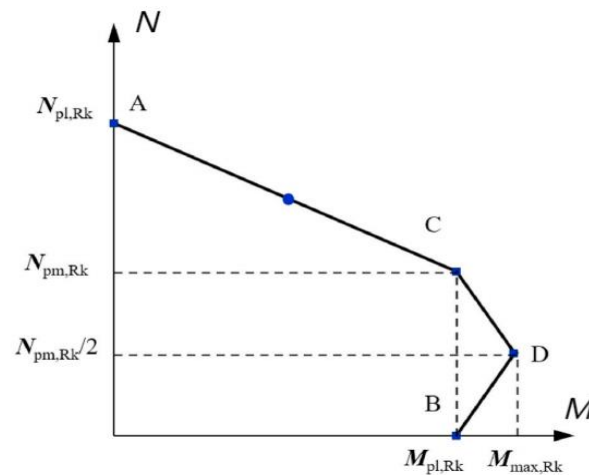


Figure 12. Simplified curve of N - M interaction in Eurocode 4.

The N - M interaction curves in Eurocode 4:

$$N_{pl} = N_{pre-a} \tag{4}$$

Due to the unique nature of the cross-sectional shape of the circular steel tube, the calculation of the pure-curved state curve requires a separate diagram, shown in Figure 13.

$$M_{pl} = 4r^2 t_s f_y \int_0^{\alpha_0} x \cos x dx + 4f_c r^2 \int_0^{\alpha_0} 1 - (\sin \alpha_0)^2 \tan x dx \tag{5}$$

$$N_{pm} = f_c \pi D^2 (74.5d - 1.25d\lambda + 9.08\lambda) \times 10^{-6} \tag{6}$$

$$M_{max} = 4r^2 t_s f_y \int_0^{\frac{\pi}{2}} x \cos x dx + 4f_c r^2 \int_0^{\frac{\pi}{2}} 1 - (\sin \alpha_0)^2 \tan x dx \tag{7}$$

where α_0 is the root of the formula $f_y \alpha_0 D_1^2 - f_c \alpha_0 D^2 \sin \alpha_0 \cos \alpha_0 = 0$.

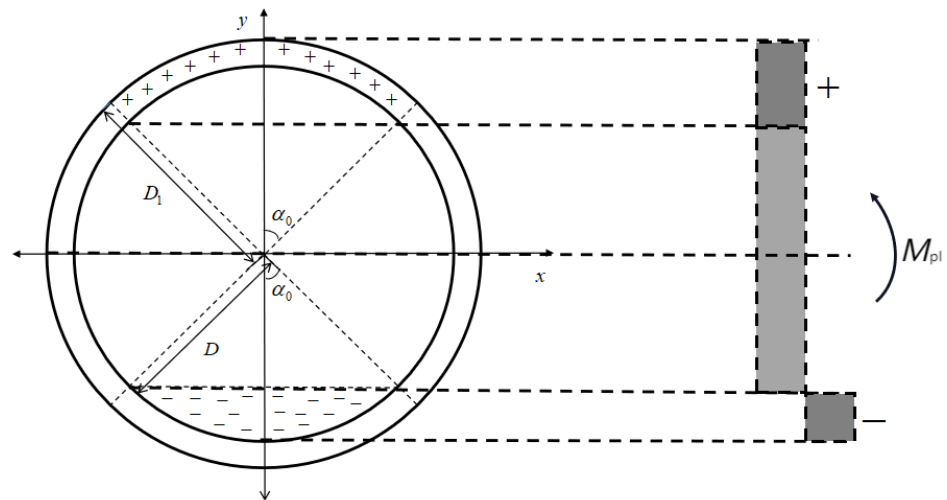


Figure 13. Calculation sketch of the bending moment with pure bending state.

The N – M interaction curves in AISC 360:

$$N_{pl} = 1.92f_y\pi(D_1^2 - D^2) \times 10^{-4} + 0.85f_c\pi D^2(74.5d - 1.25d\lambda + 9.08\lambda) \times 10^{-6} \quad (8)$$

$$M_{pl} = 4r^2t_s f_y \int_0^{\alpha_0} x \cos x dx + 3.4f_c r^2 \int_0^{\alpha_0} 1 - (\sin \alpha_0)^2 \tan x dx \quad (9)$$

$$N_{pm} = f_c \pi D^2(74.5d - 1.25d\lambda + 9.08\lambda) \times 10^{-6} \quad (10)$$

$$M_{max} = 4r^2t_s f_y \int_0^{\frac{\pi}{2}} x \cos x dx + 3.4f_c r^2 \int_0^{\frac{\pi}{2}} 1 - (\sin \alpha_0)^2 \tan x dx \quad (11)$$

where α_0 is the root of the formula $f_y\alpha_0 D_1^2 - 0.85f_c\alpha_0 D^2 \sin \alpha_0 \cos \alpha_0 = 0$.

It should be noted that stability has been considered in the calculation of N_{pre-a} , so it is not necessary to consider the stability problem again when calculating the N – M interaction curves.

Regarding the N – M interaction curves in GB 50936, unlike Eurocode 4 and AISC 360, the N – M interaction curves in GB 50936 consist of two straight lines and three key points, as shown in Figure 14.

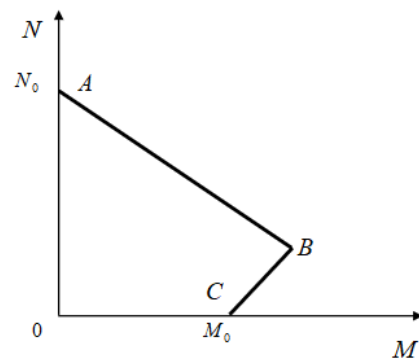


Figure 14. Simplified curve of N – M interaction in GB 50936.

The formula for N – M interaction curves for a circular concrete-filled steel tube in GB 50936 is shown below:

$$\frac{N}{\varphi_1 N_0} + 0.55 \frac{M}{\varphi_1 M_0} \leq 1 \quad (12)$$

$$\frac{1 - 4/3\varphi_1}{0.255} \frac{N}{\varphi_1 N_0} + \frac{M}{M_0} \leq 1 \quad (13)$$

$N_0 = N_{pre-a}$, $M_0 = 0.3N_{0rc}$, and r_c is the outer radius of the steel tube. ϕ_1 takes the value of 1, since M_0 and N_0 have a linear relationship, and stability has been considered in the calculation of N_{pre-a} .

We take the specific groups E2 and E4 to analyze N – M interaction curves, as shown in Figure 15.

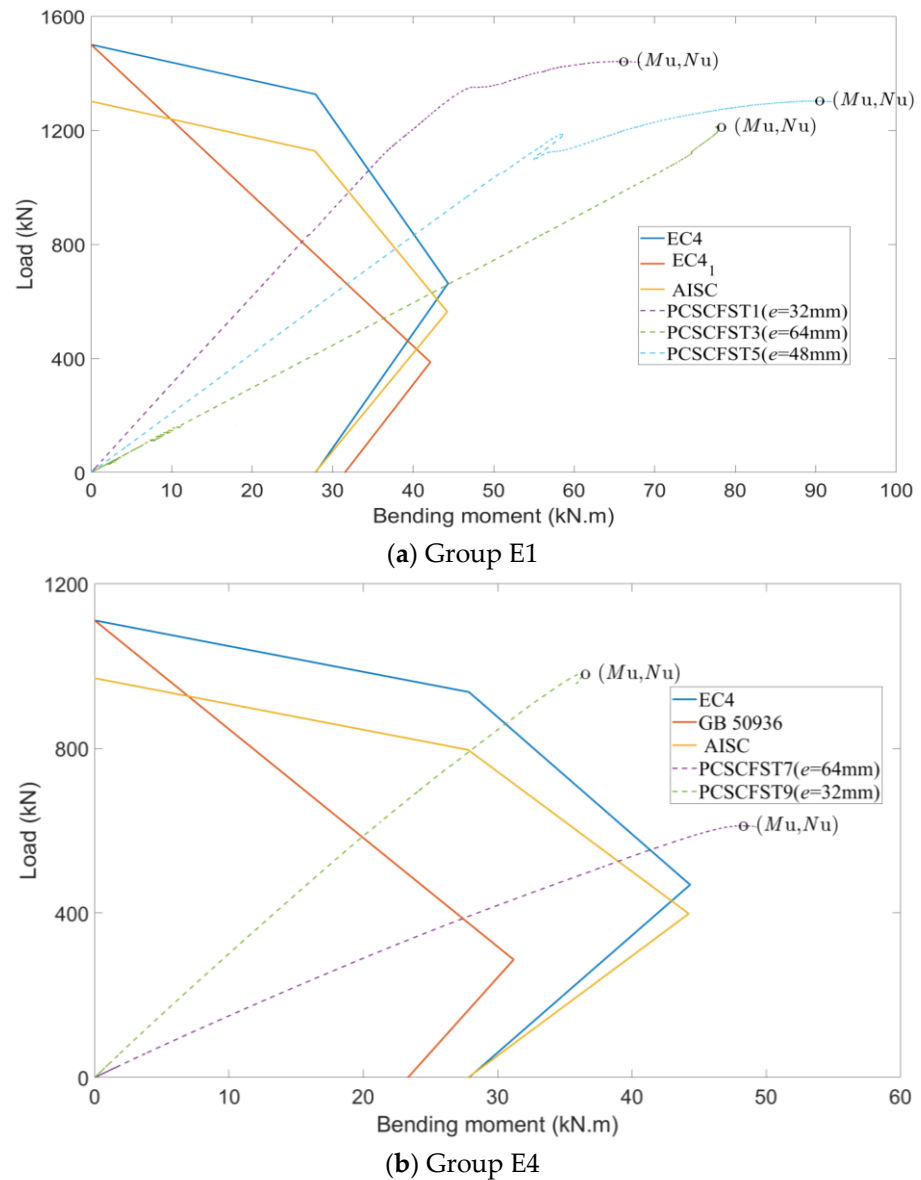


Figure 15. N – M interaction curves from Eurocode 4, AISC 360, and GB 50936.

Figure 15 displays the N – M interaction curves for the actual specimens (dashed line) and those specified by the three standards (solid line). The intersection points of the dashed and solid lines represent the ultimate bearing capacity predictions under each standard. For the examined specimens, Eurocode 4 predicts higher values than AISC 360, which, in turn, predicts higher values than GB 50936, indicating that GB 50936 has the most conservative nature, followed by AISC 360. However, the predicted values for the three standards show varied magnitudes at different locations. Table 5 lists the specific results of predicted ultimate bearing capacity, highlighting that all predictions are conservative. Consistently across all specimens, the predicted values follow the same order: Eurocode 4 > AISC 360 > GB 50936. In Eurocode 4 and AISC 360, the prediction accuracy

improves notably with an increase in slenderness ratio (from 13 to 64), a trend not observed in GB 50936.

Table 5. Predicted results for N – M interaction curves.

| Specimen No. | P_u (kN) | P_{pre-Eu} (kN) | P_{pre-As} (kN) | P_{pre-GB} (kN) | P_{pre-U} (kN) | P_{pre-Eu}/P_u | P_{pre-As}/P_u | P_{pre-GB}/P_u | P_{pre-U}/P_u |
|---------------|------------|-------------------|-------------------|-------------------|------------------|------------------|------------------|------------------|-----------------|
| PCSCFST1 | 1443 | 1064 | 983 | 807 | 1386 | 0.737 | 0.681 | 0.559 | 0.960 |
| PCSCFST2 | 1465 | 1038 | 960 | 768 | 1389 | 0.709 | 0.655 | 0.524 | 0.948 |
| PCSCFST3 | 1212 | 650 | 616 | 510 | 1260 | 0.536 | 0.508 | 0.421 | 1.040 |
| PCSCFST4 | 1296 | 749 | 708 | 533 | 1207 | 0.578 | 0.546 | 0.411 | 0.931 |
| PCSCFST5 | 1304 | 898 | 840 | 634 | 1204 | 0.689 | 0.644 | 0.486 | 0.923 |
| PCSCFST6 | 1231 | 670 | 636 | 529 | 1193 | 0.544 | 0.517 | 0.430 | 0.969 |
| PCSCFST7 | 612 | 554 | 526 | 387 | 609 | 0.905 | 0.859 | 0.632 | 0.995 |
| PCSCFST8 | 755 | 605 | 571 | 410 | 730 | 0.801 | 0.756 | 0.543 | 0.967 |
| PCSCFST9 | 981 | 860 | 793 | 583 | 957 | 0.877 | 0.808 | 0.594 | 0.976 |
| PCSCFST10 | 630 | 588 | 557 | 282 | 629 | 0.933 | 0.884 | 0.448 | 0.998 |
| Average value | -- | -- | -- | -- | -- | 0.731 | 0.686 | 0.505 | 0.971 |
| Variance | -- | -- | -- | -- | -- | 0.0196 | 0.0172 | 0.00539 | 0.00107 |

Note: P_{pre-Eu} is the prediction ultimate bearing capacity using Eurocode 4; P_{pre-As} is the prediction ultimate bearing capacity using AISC 360; P_{pre-GB} is the prediction ultimate bearing capacity using GB 50936; and P_{pre-U} is the prediction ultimate bearing capacity using Formulas (14) and (15).

4.3. The Proposed N – M Interaction Curves for PCSCFST Columns

In conclusion, the predictions from all three standards (Eurocode 4, AISC 360, GB 50936) are generally conservative and lack precision, with Eurocode 4's curve being closest to the actual ultimate bearing capacity. Consequently, modifications to Eurocode 4's N – M interaction curve are necessary for enhanced accuracy. As Chen et al. [32] identified, the external steel sleeve plays a dual role: it facilitates force transmission between the upper and lower columns and contributes to the bending moment resistance. To encapsulate these effects, parameters k_1 and k_2 are introduced to quantify the influence of the external steel sleeve on bending moments, while b_1 and b_2 account for the impact of the bolt diameter, and c_1 and c_2 account for the ratio of external sleeve thickness to steel tube thickness. These modifications refine Eurocode 4's bending moment values, resulting in a more precise N – M interaction curve. The revised formula is provided below.

$$M_{pl} = 4b_1c_1k_1r^2t_s f_y \int_0^{\alpha_0} x \cos x dx + 4b_1c_1k_1f_c r^2 \int_0^{\alpha_0} 1 - (\sin \alpha_0)^2 \tan x dx \quad (14)$$

$$M_{max} = 4r^2b_2c_2k_2t_s f_y \int_0^{\frac{\pi}{2}} x \cos x dx + 4b_2c_2k_2f_c r^2 \int_0^{\frac{\pi}{2}} 1 - (\sin \alpha_0)^2 \tan x dx \quad (15)$$

where when $\lambda \leq 13$, $k_1 = 2.6$, $k_2 = 2.3$; when $\lambda > 13$, $k_1 = 1.55$ and $k_2 = 1.3$; when $d \leq 12$, $b_1 = b_2 = 1$; when $d > 12$, $b_1 = 0.9$ and $b_2 = 0.88$; when $|1 - t_1/t_2| \leq 0.2$, $r_1 = r_2 = 1$; and when $|1 - t_1/t_2| > 0.2$, $b_1 = 0.9$, and $b_2 = 0.88$.

The predicted results are shown in Table 5. The average value of P_{pre-U}/P_u is 0.971, and the variance is 0.00107. The modified formula has a high accuracy in predicting the ultimate bearing capacity.

5. Conclusions

The study explored the mechanical behavior of precast circular semi-continuous concrete-filled steel tube (PCSCFST) columns under uniaxial eccentric compression, analyzing the impacts of various parameters such as the eccentric distance, slenderness ratio, bolt thickness, steel tube thickness, and external steel sleeve thickness. The key findings are summarized below:

- (1) The failure mode in columns with a high slenderness ratio ($\lambda = 64$) is characterized primarily by overall bending with no significant local bulging. In contrast, columns with a low slenderness ratio ($\lambda = 13$) exhibit more pronounced local bulging, particularly between the external steel sleeve and the end plate.

- (2) The thickness and diameter of both the external steel sleeve and the bolts must be kept within reasonable limits. Excessive thickness in the steel tube can easily cause the bolts to yield, leading to connection failure and reduced load-bearing capacity, while an excessively large bolt diameter can alter the force transmission mode of the bolt–sleeve connection, resulting in a reduced ultimate bearing capacity.
- (3) The coordination among components in short columns is less effective compared to in long columns. Through the bolt–sleeve connection method, each component influences the others under load. Therefore, it is crucial to maintain the external steel sleeve’s wall thickness and the bolt’s diameter within a specific range to ensure optimal coordination among the components.
- (4) The predictions of the ultimate bearing capacity using N – M interaction curves from Eurocode 4, AISC 360, and GB 50936 proved conservative, with Eurocode 4 being the most accurate and GB 50936 the most conservative. The accuracy of predictions from Eurocode 4 and AISC 360 notably improves with an increased slenderness ratio, a trend not observed with GB 50936.
- (5) A more accurate prediction method is obtained according to Eurocode 4, with the average value and variance of P_{pre-U}/P_u being 0.971 and 0.00107, respectively.

Author Contributions: Project administration, B.C.; funding acquisition, B.C.; writing—original draft, L.Z.; data curation, L.Z.; writing—review and editing, H.Q.; validation, H.Q.; methodology, Z.P.; investigation, Z.P. All authors have read and agreed to the published version of the manuscript.

Funding: This research was funded by the University Natural Science Research Project of Anhui Province (No. KJ2020A0366) and the Key Research and Development Program of Anhui Province (No. 2022o07020003) and the Open Project of Engineering Research Center of Anhui Metallurgical Solid Waste Green Construction (No. YJGF002-2024) and the Science and Technology Planning Project of Guichi District, Chizhou City (No. GCKJ202210).

Data Availability Statement: The data presented in this study are available upon reasonable request from the corresponding author. Requests for access to these data should be directed to [caobing.0427@ahpu.edu.cn], specifying the intended use and any necessary conditions.

Acknowledgments: The authors express their sincere gratitude to all who provided invaluable assistance throughout this research. Special thanks are extended to the technical staff and our colleagues at Anhui Polytechnic University and Engineering Research Center of Anhui Green Building and Digital Construction and Engineering Research Center of Anhui Metallurgical Solid Waste Green Construction for their expert advice and support. We also appreciate the constructive feedback from the anonymous reviewers, which significantly enhanced the quality of this manuscript.

Conflicts of Interest: Author Zhicheng Pan was employed by the companies Sinohydro Engineering Bureau 8 Co., Ltd. and Power China Chizhou Changzhi Prefabricated Construction Co., Ltd. The remaining authors declare that the research was conducted in the absence of any commercial or financial relationships that could be construed as a potential conflict of interest.

References

1. Wang, Y.H.; Tang, Q.; Su, M.N.; Tan, J.K.; Wang, W.Y.; Lan, Y.S.; Luo, W.; Zhou, Y. Post-earthquake fire performance of square concrete-filled steel tube columns. *Thin-Walled Struct.* **2020**, *154*, 106873. [[CrossRef](#)]
2. Zhao, P.; Huang, Y.; Liu, Z.; Wang, H.; Lu, Y. Experimental research on seismic performance of steel fiber-reinforced recycled concrete-filled circular steel tube columns. *J. Build. Eng.* **2022**, *54*, 104683. [[CrossRef](#)]
3. Ding, C.; Bai, Y.; Yang, K.; Zhang, J. Cyclic behavior of prefabricated connections for a steel beam to concrete-filled steel tube column. *J. Constr. Steel Res.* **2021**, *176*, 106422. [[CrossRef](#)]
4. Li, Y.L.; Chan, T.M.; Zhao, X.L. Review on blind bolted connections to concrete-filled steel tubes. *Thin-Walled Struct.* **2023**, *183*, 110444. [[CrossRef](#)]
5. Rehmat, S.; Sadeghnejad, A.; Mantawy, I.M.; Azizinamini, A. Experimental study on concrete-filled steel tubes to footing connection using ultra-high performance concrete. *Eng. Struct.* **2021**, *242*, 112540. [[CrossRef](#)]
6. Zhu, G.; Ma, Y.X.; Tan, K.H. Experimental and analytical investigation on precast concrete-encased concrete-filled steel tube column-to-column dry connections under axial tension. *Structures* **2022**, *45*, 523–541. [[CrossRef](#)]
7. Ding, C.; Pan, X.; Bai, Y.; Shi, G. Prefabricated connection for steel beam and concrete-filled steel tube column. *J. Constr. Steel Res.* **2019**, *162*, 105751. [[CrossRef](#)]

8. Jiao, C.; Liu, W.; Li, Y.; Shi, W.; Long, P. Experimental study of CFST embedded precast concrete bridge column-foundation connection with studs. *Soil Dyn. Earthq. Eng.* **2023**, *168*, 107826. [[CrossRef](#)]
9. Song, S.S.; Xu, F.; Chen, J.; Wang, Y.H. Mechanism of load introduction and transfer within steel-encased concrete-filled steel tube connections. *J. Constr. Steel Res.* **2023**, *203*, 107818. [[CrossRef](#)]
10. Zhou, X.; Xu, T.; Liu, J.; Wang, X.; Chen, Y.F. Seismic performance of concrete-encased column connections for concrete-filled thin-walled steel tube piers. *Eng. Struct.* **2022**, *269*, 114803. [[CrossRef](#)]
11. Xu, T.; Zhang, S.; Liu, J.; Wang, X. Design method of concrete-filled thin-walled steel tube column-foundation connections. *Eng. Struct.* **2021**, *246*, 113033. [[CrossRef](#)]
12. Ansari, M.; Jeddi, M.Z.; Badaruzzaman, W.H.W.; Tahir, M.M.; Osman, S.A.; Hosseinpour, E. A numerical investigation on the through rib stiffener beam to concrete-filled steel tube column connections subjected to cyclic loading. *Eng. Sci. Technol. Int. J.* **2021**, *24*, 728–735. [[CrossRef](#)]
13. Jiang, L.; Liu, Y.; Fam, A.; Liu, B.; Pu, B.; Zhao, R. Experimental and numerical analyses on stress concentration factors of concrete-filled welded integral K-joints in steel truss bridges. *Thin-Walled Struct.* **2023**, *183*, 110347. [[CrossRef](#)]
14. Sun, L.; Liu, Y.; Wang, H.; Shi, F. Local and post-local buckling behavior of welded square high-strength steel tubes with concrete-infilled restraints. *Thin-Walled Struct.* **2023**, *183*, 110381. [[CrossRef](#)]
15. Liu, W.H.; Guo, Y.L.; Tian, Z.H.; Yang, X.; Li, J.Y. Experimental and numerical study of T-shaped irregularly concrete-filled steel tube columns under combined axial loads and moments. *J. Build. Eng.* **2023**, *65*, 105796. [[CrossRef](#)]
16. Lin, Y.; Ye, Q.; Wang, Y.; Shu, C.; Zhang, F.; Zhang, Y.; Zhao, Y.; Cao, H. Seismic behavior of diaphragm-through bolted-welded joints between CFST column to steel beam. *J. Constr. Steel Res.* **2023**, *200*, 107651. [[CrossRef](#)]
17. Tong, G.H.; Hu, Z.Z.; Chen, Y. Study on the moment capacity of a connection joining an I-beam to concrete-filled multicellular steel tube walls. *J. Constr. Steel Res.* **2021**, *182*, 106643. [[CrossRef](#)]
18. Parvari, A.; Zahrai, S.M.; Mirhosseini, S.M.; Zeighami, E. Numerical and experimental study on the behavior of drilled flange steel beam to CFT column connections. *Structures* **2020**, *28*, 726–740. [[CrossRef](#)]
19. Doung, P.; Leelataviwat, S.; Sasaki, E. Tensile strength and failure mechanism of internal diaphragms in wide flange beam-to-box column connections with concrete filling. *J. Build. Eng.* **2021**, *34*, 102037. [[CrossRef](#)]
20. Ng, W.H.; Kong, S.Y.; Chua, Y.S.; Bai, Y. Tensile behavior of innovative one-sided bolts in concrete-filled steel tubular connections. *J. Constr. Steel Res.* **2022**, *191*, 107165. [[CrossRef](#)]
21. Wu, L.Y.; Chung, L.L.; Tsai, S.F.; Shen, T.J.; Huang, G.L. Seismic behavior of bolted beam-to-column connections for concrete-filled steel tube. *J. Constr. Steel Res.* **2005**, *61*, 1387–1410. [[CrossRef](#)]
22. Gan, D.; Zhang, Y.; Zhou, X.; Ba, Z.; Li, D.; Hou, Z.; Uy, B. Seismic performance of concrete-filled steel tubular column connections using blind bolts. *J. Constr. Steel Res.* **2023**, *207*, 107947. [[CrossRef](#)]
23. Yang, Y.; Liao, F.; Tao, Z.; Zhang, C.; Gao, X. Compressive and flexural behavior of prefabricated concrete-filled steel tubular columns with bolted splices. *J. Constr. Steel Res.* **2022**, *188*, 107048. [[CrossRef](#)]
24. *GB/T 50107-2010*; Standard for Evaluation of Concrete Compressive Strength. China Architecture and Building Press: Beijing, China, 2010.
25. *GB/T 228-2010*; Metallic Materials-Tensile Testing at Ambient Temperature. Standards Press of China: Beijing, China, 2010.
26. Cao, B.; Xie, M.; Zhu, L.; Cao, W.; Huang, B.; Du, Y.; Wang, J.; Yang, Y.; Wang, C. Axial compression behavior of precast circular semi-continuous concrete-filled steel tube columns. *Adv. Mech. Eng.* **2022**, *14*, 16878132221107471. [[CrossRef](#)]
27. Feng, P.; Cheng, S.; Bai, Y.; Ye, L. Mechanical behavior of concrete-filled square steel tube with FRP-confined concrete core subjected to axial compression. *Compos. Struct.* **2015**, *123*, 312–324. [[CrossRef](#)]
28. Cheng, G.; Zhou, X.; Liu, J.; Chen, Y.F. Seismic Behavior of circular tub steel-reinforced concrete column to steel beam connections. *Thin-Walled Struct.* **2019**, *138*, 485–495. [[CrossRef](#)]
29. *Eurocode 4, EN 1994-1-1*; Design of Composite Steel and Concrete Structures, Part 1.1. General Rules and Rules for Buildings. British Standards Institution: London, UK, 2004.
30. *ANSI/AISC 360-10*; Specification for Structural Steel Buildings. American Institute of Steel Construction: Chicago, IL, USA, 2010.
31. *GB50936-2014*; Technical Code for Concrete Filled Steel Tubular Structures. Standard Press of China: Beijing, China, 2014.
32. Chen, Y.; Wang, C.L.; Wang, C.; Zeng, B. Experimental study and performance evaluation of compression members in space structures strengthened with assembled external steel sleeves. *Thin-Walled Struct.* **2022**, *173*, 108999. [[CrossRef](#)]

Disclaimer/Publisher's Note: The statements, opinions and data contained in all publications are solely those of the individual author(s) and contributor(s) and not of MDPI and/or the editor(s). MDPI and/or the editor(s) disclaim responsibility for any injury to people or property resulting from any ideas, methods, instructions or products referred to in the content.